# Magnetic field-assisted solidification of W319 Al alloy qualified by high-speed synchrotron tomography

Song, Zihan; Boller, Elodie; Rack, Alexander; Lee, Peter D; Cai, Biao

*DOI:*
10.1016/j.jallcom.2022.168691



*Document Version*
Publisher's PDF, also known as Version of record

*Citation for published version (Harvard):*
Song, Z, Boller, E, Rack, A, Lee, PD & Cai, B 2023, 'Magnetic field-assisted solidification of W319 Al alloy qualified by high-speed synchrotron tomography', *Journal of Alloys and Compounds*, vol. 938, 168691. https://doi.org/10.1016/j.jallcom.2022.168691

Journal of Alloys and Compounds 938 (2023) 168691

Contents lists available at ScienceDirect

Journal of Alloys and Compounds

journal homepage: www.elsevier.com/locate/jalcom

# Magnetic field-assisted solidification of W319 Al alloy qualified by high-speed synchrotron tomography

Zihan Song [a], Elodie Boller [b], Alexander Rack [b], Peter D. Lee [c], Biao Cai [a,*]

[a] School of Metallurgy and Materials, University of Birmingham, B15 2TT, UK
[b] ESRF-The European Synchrotron, 71 Avenue des Martyrs, 380 00 Grenoble, France
[c] Mechanical Engineering, University College London, London WC1E 7JE, UK

ARTICLE INFO

*Article history:*
Received 11 September 2022
Received in revised form 13 December 2022
Accepted 30 December 2022
Available online 31 December 2022

*Keywords:*
Al alloys
Intermetallic compounds
Synchrotron X-ray tomography
Magnetic field-assisted solidification

ABSTRACT

Magnetic fields have been widely used to control solidification processes. Here, high-speed synchrotron X-ray tomography was used to study the effect of magnetic fields on solidification. We investigated vertically upward directional solidification of an Al-Si-Cu based W319 alloy without and with a transverse magnetic field of 0.5 T while the sample was rotating. The results revealed the strong effect of a magnetic field on both the primary α-Al phase and secondary β-$Al_5FeSi$ intermetallic compounds (IMCs). Without the magnetic field, coarse primary α-Al dendrites were observed with a large macro-segregation zone. When a magnetic field is imposed, much finer dendrites with smaller primary arm spacing were obtained, while macro-segregation was almost eliminated. Segregated solutes were pushed out of the fine dendrites and piled up slightly above the solid/liquid interface, leading to a gradient distribution of the secondary β-IMCs. This work demonstrates that rotating the sample under a transversal magnetic field is a simple yet effective method to homogenise the temperature and composition distributions, which can be used to control the primary phase and the distribution of iron-rich intermetallics during solidification.


## 1. Introduction

Compared with the primary aluminium production from bauxite core, secondary aluminium ingots produced from recycled aluminium scraps, including end-of-life automotive and used beverage cans, can save up to 95% of the energy [1]. However, impurities such as Iron and Silicon accumulate during the recycling process [2]. Iron in particular is expensive to remove. Further, iron has a very low solid solubility (max 0.05 wt%) in aluminium [3] and can form hard and brittle Fe-rich intermetallic compounds (IMCs) such as $Al_{13}Fe_4$ [4,5] and β-$Al_5FeSi$ [6]. Their morphologies, sizes and distribution, if not controlled, can negatively impact castability [7] and reduce mechanical and corrosion properties of the final components[8,9]. IMCs in aluminium alloys can be controlled by their crystal structures and solidification conditions such as cooling rates, temperature gradients and external fields (e.g. mechanical shearing, ultrasonic processing, or magnetic stirring) [10–14].

Synchrotron X-ray radiography has been widely used to reveal the growth process of various IMCs in Al alloys during solidification, for instance, α-Al(FeMnCr)Si in Al-Si-Cu alloys [15] and $Al_{13}Fe_4$ in Al-3%Fe alloys [4,16]. Recently, high-speed synchrotron X-ray tomography has been developed allowing us to unravel the microstructures in 4D (3D plus time) [17–22], and the approach was applied to study Fe-rich intermetallics in Al alloys. Terzi et al. [19] reported the growth of irregular α-Al/β-$Al_5FeSi$ eutectic. Cai et al. [20] studied the coupled growth of primary α-Al and secondary β-phase in W319 alloy, which found that the growth rates and sizes of β-phase were restricted by the available inter-primary dendritic space. Puncreobutr et al. [21] illustrated the secondary β-phase has great effects on blocking liquid flows and decreasing the permeability of the semi-solid Al-Si-Cu alloys. Cao et al. [22] have revealed the growth process of the primary Fe-rich IMCs with and without a weak magnetic field (0.07 T) of Al-Si-Fe alloy. Those examples show the power of high-speed synchrotron tomography coupled with advanced imaging processing and numerical simulation to study the growth dynamics and kinetics of Fe-rich IMCs in Al alloys.

Magnetic fields have been widely used in altering fluid flows during solidification processes [23–28], making use of physical effects including electromagnetic damping [29,30], electromagnetic stirring [31,32] and thermoelectric magnetohydrodynamic (TEMHD) [33,34]. Previous studies showed that when applying a rotating magnetic field, both the temperature and solute distribution can be homogenised during solidification, leading to structure refinement of the primary α-Al phase [26,35]. However, several questions

* Corresponding author.
*E-mail address:* b.cai@bham.ac.uk (B. Cai).

https://doi.org/10.1016/j.jallcom.2022.168691

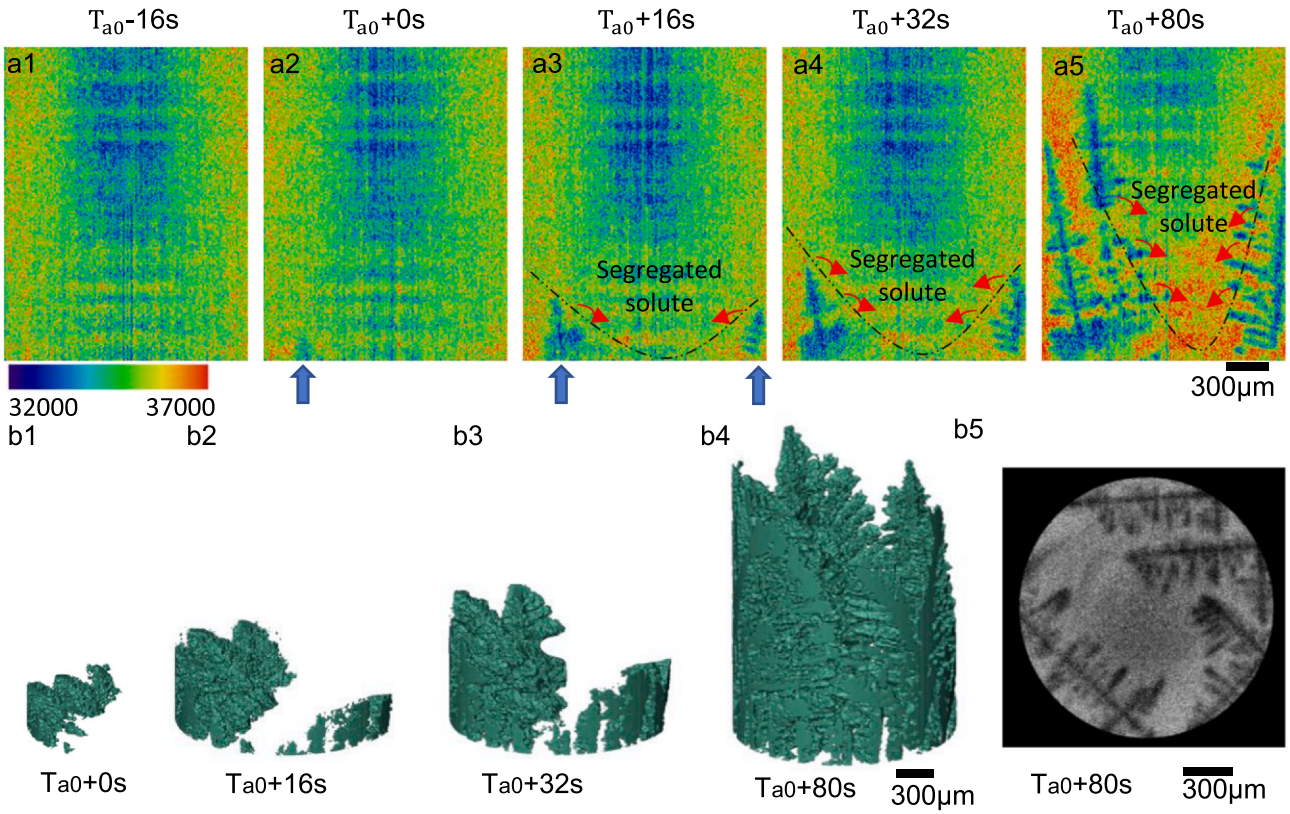


**Fig. 1.** (a) 2D vertical slices of α-Al phase at different timestamps (B= 0 T, TG= 2.5 ℃/*mm*, CR= 0.1℃/*s*); (b1-b4) 3D volumes of α-Al phase at different timestamps; (b5) a horizontal slice at the height of 1.1 mm.

remain unanswered. Will the modified morphologies of the solidification microstructure influence the permeability in the mushy zone? In Al-Si-Cu based alloys, as the β-intermetallic is the secondary phase following the primary α-Al phase [20], will the growth behaviours of β-IMCs be influenced by the application of magnetic fields? In view of these questions, the present study aims to reveal the growth dynamics of both the primary α-Al phase and secondary β-IMC during solidification of W319 (Al-Si-Cu based) alloys under a constant transversal magnetic field of 0.5 T while the sample is rotating via high-speed synchrotron tomography. Then we calculated the absolute permeability of the solidified structures using image-based simulation with and without the presence of the β intermetallic compounds under different solidification conditions. The results can be used to validate simulation models, especially the growth behaviours of secondary IMCs during the casting of aluminium alloys. It also demonstrates that a magnetic field can be used to control the distribution of iron-rich intermetallics.

## 2. Materials and methods

The Al-Si-Cu alloy W319 (Al-5.50Si-3.40Cu-0.87Fe-0.27Mg, in weight per cent) was provided by Ford Motor Company. The alloy is frequently used in engines such as engine blocks and cylinder heads [36]. Cylindrical specimens with diameters of 1.8 mm and lengths of 100 mm were cut via wire electrical discharge machining. Each sample was placed into an alumina tube with a 2 mm inner diameter and 3 mm outer diameter. A bespoke temperature gradient furnace (MagDS) [20,37] was used to perform the solidification experiment. MagDS furnace consists of a small bespoke temperature gradient stage and a magnet yoke, which was used to control the solidification conditions (cooling rates (CR), temperature gradients (TG) and the strength of the magnetic field (B)). Two experiments were performed. In the first experiment, the sample was heated up until melting. The specimen was then held at the melting state for 20 min before it was cooled at a constant rate (CR) of 0.1℃/s until fully solidified [26]. A temperature gradient (TG) 2.5℃/mm was applied to the specimen (the top part was set at a higher temperature). In the second experiment, the magnet yoke was installed close to the furnace, which was able to produce a transverse magnetic field of B = 0.5 T. The solidification experiment was carried out using the same heating and cooling conditions. Thereby, solidification condition I is B = 0 T, CR = 0.1℃/s, TG=2.5℃/mm, whereas solidification condition II is B = 0.5 T, CR = 0.1℃/s, TG=2.5℃/mm. In both conditions, the samples were rotating continuously during cooling for tomography.

The *in situ* solidification experiments were performed at the ID19 beamline of the European Synchrotron Radiation Facility (ESRF), with a 31 keV pink X-ray beam [38]. A high-resolution high-speed detector (PCO.dimax) was used, achieving a pixel size of 2.2 μm, and a field of view (FOV) of 2.2 × 2.2 $mm^2$. During solidification, rapid tomographic images were acquired when the sample was rotating at a speed of π(rad/s) continuously. Each tomogram required a collection time of 1 s and was composed of 1000 projections (radiography), collected over 180°. Another 15 s of waiting time were consumed for downloading the tomograms between two consecutive scans.

For absorption contrast-based synchrotron X-ray tomography, the phases with higher density (higher absorption coefficients) have higher grey values [39,40], allowing the distributions of density/composition before and during solidification to be mapped. Using this concept, we have plotted the 2D vertical slices with an artificial colour map based on 16-bit unit images. In this work, the regions with low attenuation values are shown in blue and green (e.g. in Fig. 1-a), which normally mean a higher concentration of light elements such as Al and Si in this experiment. Conversely, yellow to red regions should contain heavier elements such as Fe and Cu, which strongly attenuate the X-rays.

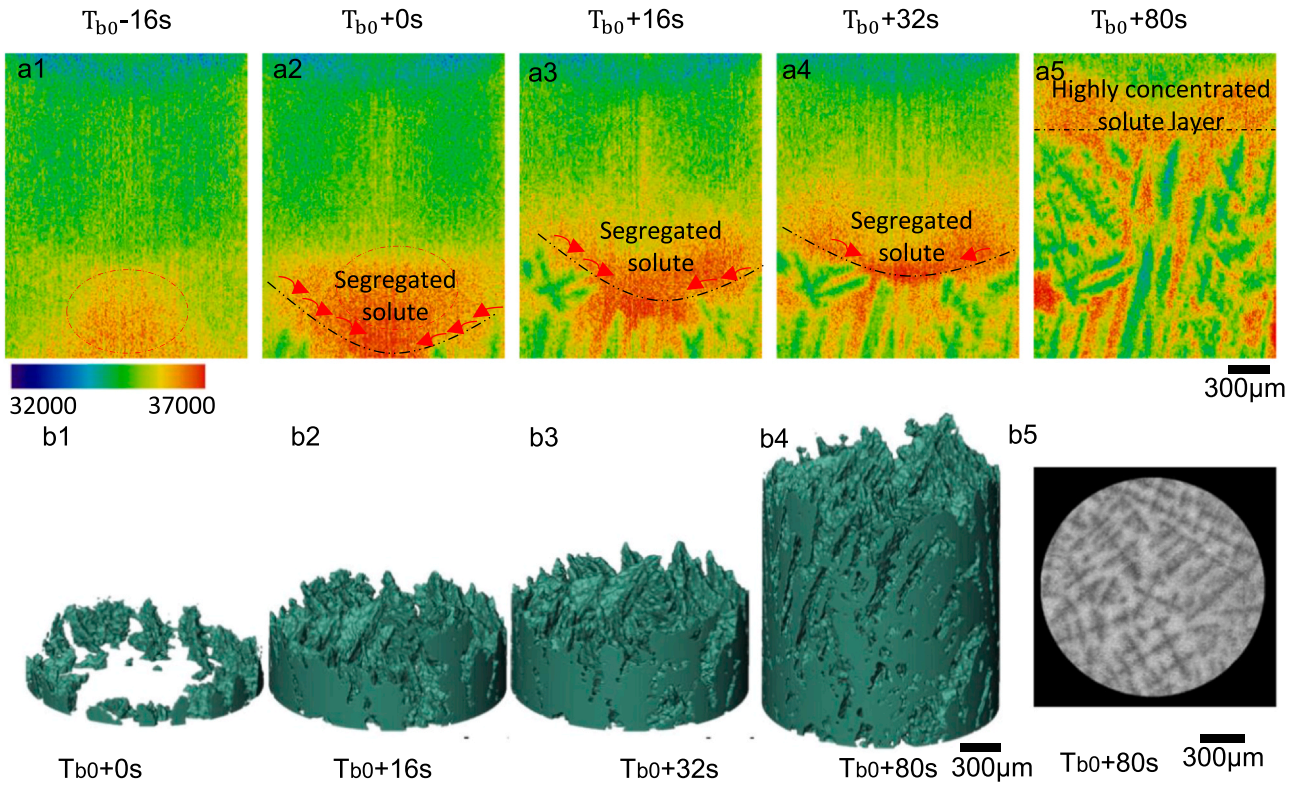


**Fig. 2.** (a) 2D vertical slices of α-Al phase at different timestamps (B= 0.5 T, TG= 2.5℃/*mm*, CR= 0.1℃/*s*); (b1-b4) 3D volumes of α-Al phase at different timestamps; (b5) a horizontal slice at height of 1.1 mm.

Avizo 2020.1 (Thermo Fisher, U.S.) was used to segment and quantify the phases and perform the absolute permeability simulation. For the primary α-Al phase, 3D anisotropic diffusion was chosen to reduce the noises [41], followed by the function of interactive thresholding whose values were based on the Ostu method implemented in ImageJ [42]. To segment the secondary β-$Al_5FeSi$ IMCs, 3D anisotropic diffusion and morphological Laplacian filters were employed. More details about image processing can be found in the supplementary note. Absolute permeability was calculated by solving the Stokes equations as shown below using the Avizo XlabSuite Extension toolbox [43].

$$\vec{\nabla}.\vec{V_L} = 0 \quad (1)$$

$$\mu_L \nabla^2 \vec{V_L} - \vec{\nabla} P_L = \vec{0} \quad (2)$$

Where $\vec{V_L}$ is the velocity of the fluid, $\mu_L$ is the dynamic viscosity of the fluid, $\vec{\nabla}.$ Is the divergence operator, $\vec{\nabla}$ is the gradient operator, $\nabla^2$ is the Laplacian operator and $P_L$ is the pressure of the fluid.

8 groups of tomographic data from each experiment were chosen. Sub-volumes of 882× 882× 882 $\mu m^3$ from the bottom centre of the FOV were cropped out for the simulation. Inlet flow along the vertical direction provided the permeability of fluid to flow parallel to the primary dendritic arms as the dendrites were aligned with the vertical direction of the samples. The flow simulations were set with the input pressure of 1.3 bar and the output pressure of atmospheric pressure by default. The fluid viscosity was set to be 0.001 Pa.s [6,21].

## 3. Results and discussion

### 3.1. α-Al phase

Fig. 1 shows the growth process of the primary α-Al phase without a magnetic field under the solidification condition (condition I) in the first 80 s (videos 1-a and 1-b). Figs. 1-a1 is the slice captured 16 s before the dendrites were observed within the FOV. The periphery of the sample shows higher image contrast, indicating heavier elements were driven to the periphery to form a macro-segregation zone, possibly due to the centripetal force resulting from the sample rotation during the holding period (20 min). As a positive vertical temperature gradient (TG) of2.5℃/mm was applied during cooling (a lower temperature at the bottom of the FOV), columnar dendrites appeared at the bottom of the FOV and grew upwards. The dendrites grew from the left side of the FOV first (Figs. 1-a2 and 1-b1). 16 s later, a few more dendrites appeared on the bottom right side. These dendrites then branched toward the centre region of the FOV (Figs. 1-a3 and b2). Well-developed large dendritic trunks with both secondary and tertiary arms formed after 80 s (Figs. 1-a5 and 1-b4). As shown in Figs. 1-a5, there is a large region (27.8% cross-section area fraction based on Figs. 1-b5) free of dendrite in the middle of the sample, resulting in a very uneven, concave solid-liquid interface and a macro-segregation of Cu, reducing the solidification temperature in this region. The angle between the solid/liquid interface and the horizontal direction is around 70º.

Supplementary material related to this article can be found online at doi:10.1016/j.jallcom.2022.168691.

During solidification, solute elements such as Cu, Fe and Si would be ejected into the melt. Due to the gravity effect [37], heavy elements (Cu and Fe) accumulated in the free space in the middle and bottom of the sample, leading to the macro-segregation zone that shows in yellow and red (high grey values) in Figs. 1-a5. This solute accumulation restricted dendrites from growing into this region, as observed in Figs. 1-a3 and Figs. 1-b2, leading to the formation of a curved solid/liquid interface. This curved interface became more severe as more Cu and Fe atoms are ejected into the central region of the sample (Figs. 1-a4 and a5). The secondary arms of existing dendrites branch into this zone at the later stage of solidification

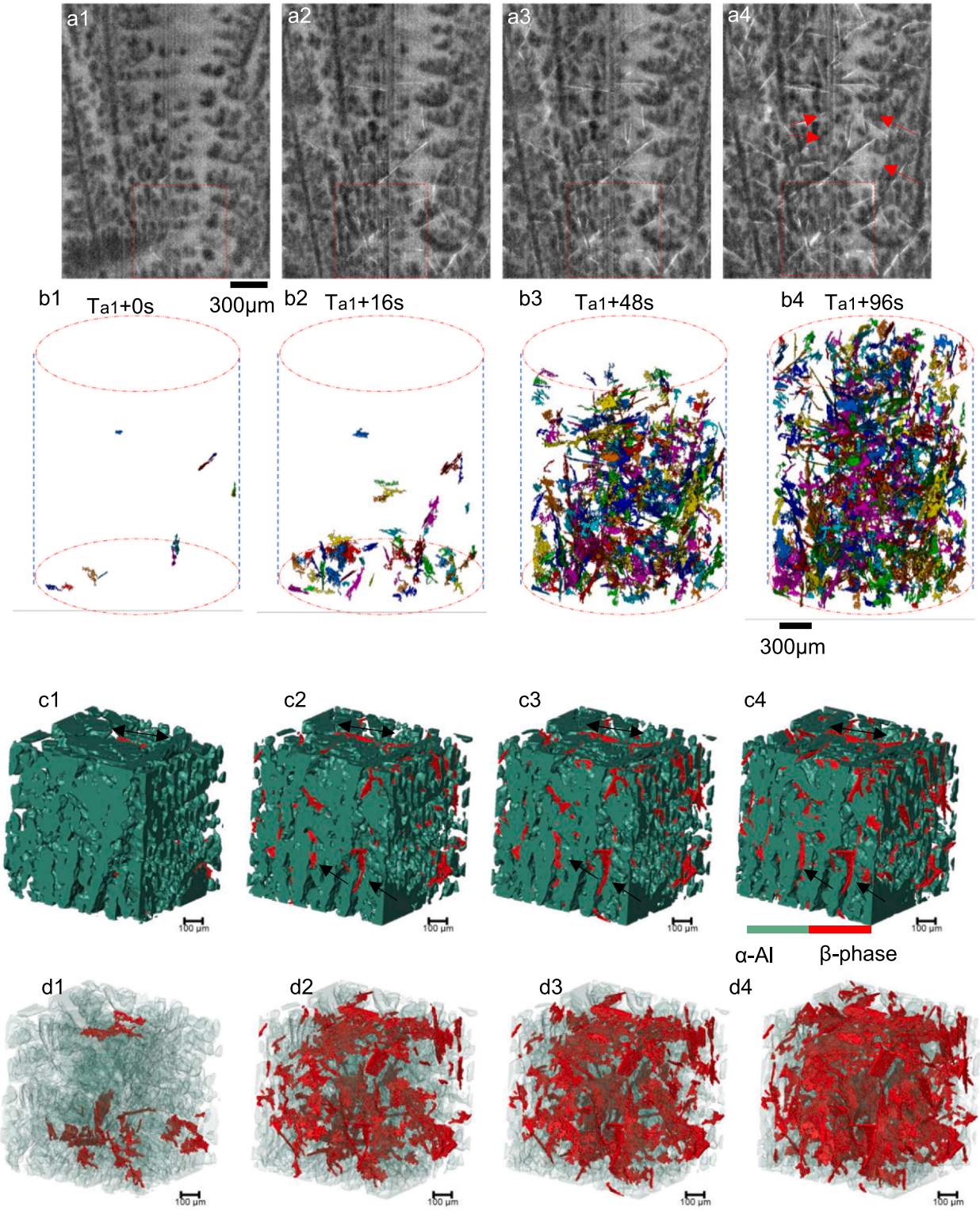


**Fig. 3.** (a) 2D vertical slices of β -phase at different timestamps (B= 0 T, TG= 2.5℃/*mm*, CR= 0.1℃/*s*); (b) 3D volumes of β-phase at different timestamps; Cropped region (882× 882× 882 $\mu m^3$) from Fig. 2-a at different timestamps. (c) 3D volumes (d) 3D volume with transparent α-Al phase.

after the temperature has decreased further, forming well-developed dendritic structures (Figs. 1-b4 and b5).

For solidification condition II with the application of a transversal 0.5 T magnetic field, Cu and Fe elements were shown to be concentrated at the bottom centre of the FOV before solidification (Figs. 2-a1, red circle). This segregation was eased, as solidification progressed (Figs. 2-a2 to a4). The solid/liquid interface (black dashed line) was initially a curved one (Figs. 2-a2) but gradually transitioned to be flat within 64 s (in video 2-a) as the solidification continued. Multiple dendrites were formed as shown in Figs. 2-b1. They grew upwards slightly tilted from the vertical direction. Figs. 5a and 5b show the growth orientation of α-Al dendrites in solidification conditions I and II, respectively. We manually selected the primary arm of the dendrites and represent them as cylinders, which allows

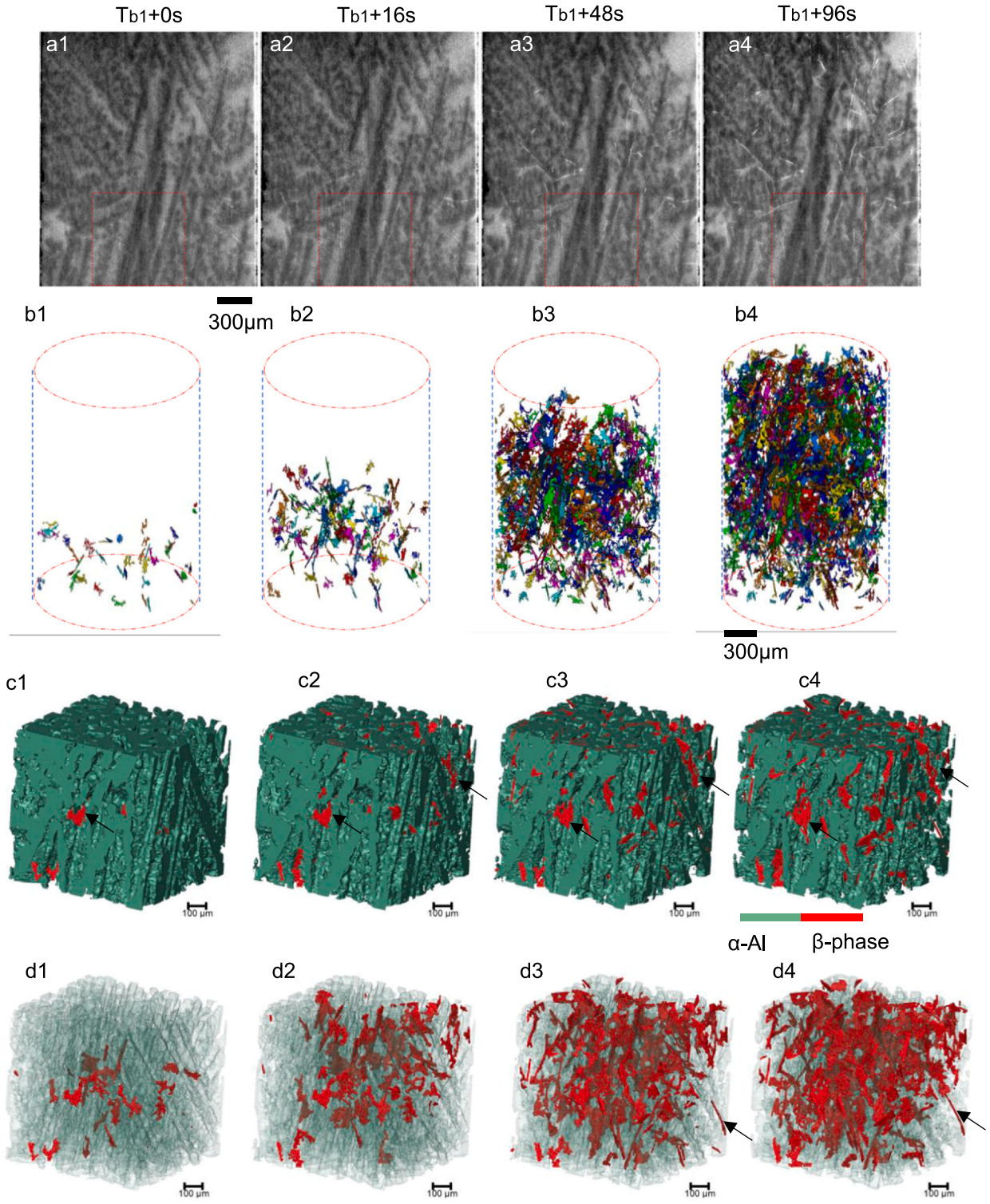


**Fig. 4.** (a) 2D vertical slices of β-phase at different timestamps (B= 0.5 T, TG= 2.5℃/*mm*, CR= 0.1℃/*s*); (b) 3D volumes of β-phase at different timestamps; Cropped region(882× 882× 882 $\mu m^3$) from Fig. 3-a at different timestamps (c) 3D volumes (d) 3D volume with transparent α-Al phase.

us to measure the titling angle (φ), which is the angle between the direction of the length of cylinders and the vertical direction (Z) of the sample. Without the magnetic field, 5 out of 6 dendrites grew almost parallel to the vertical direction of the sample with tilted angles between 3º and 17º (Fig. 5a). The remaining dendrite grew with a large tilting angle of 37º. Under the magnetic field, we have selected 41 dendrites as representatives. They grew upwards with tilting angles (Fig. 5-b1) ranging from 6º to 37º. In Fig. 5-b2, it seems the dendrites grew with a pattern: some in the centre of the specimen in a clockwise direction as pointed by red arrows, while some in an anti-clockwise direction as pointed by blue arrows in the peripheral. This behaviour might be attributed to the solute flow caused by the application of the magnetic field and sample rotation.

Supplementary material related to this article can be found online at doi:10.1016/j.jallcom.2022.168691.

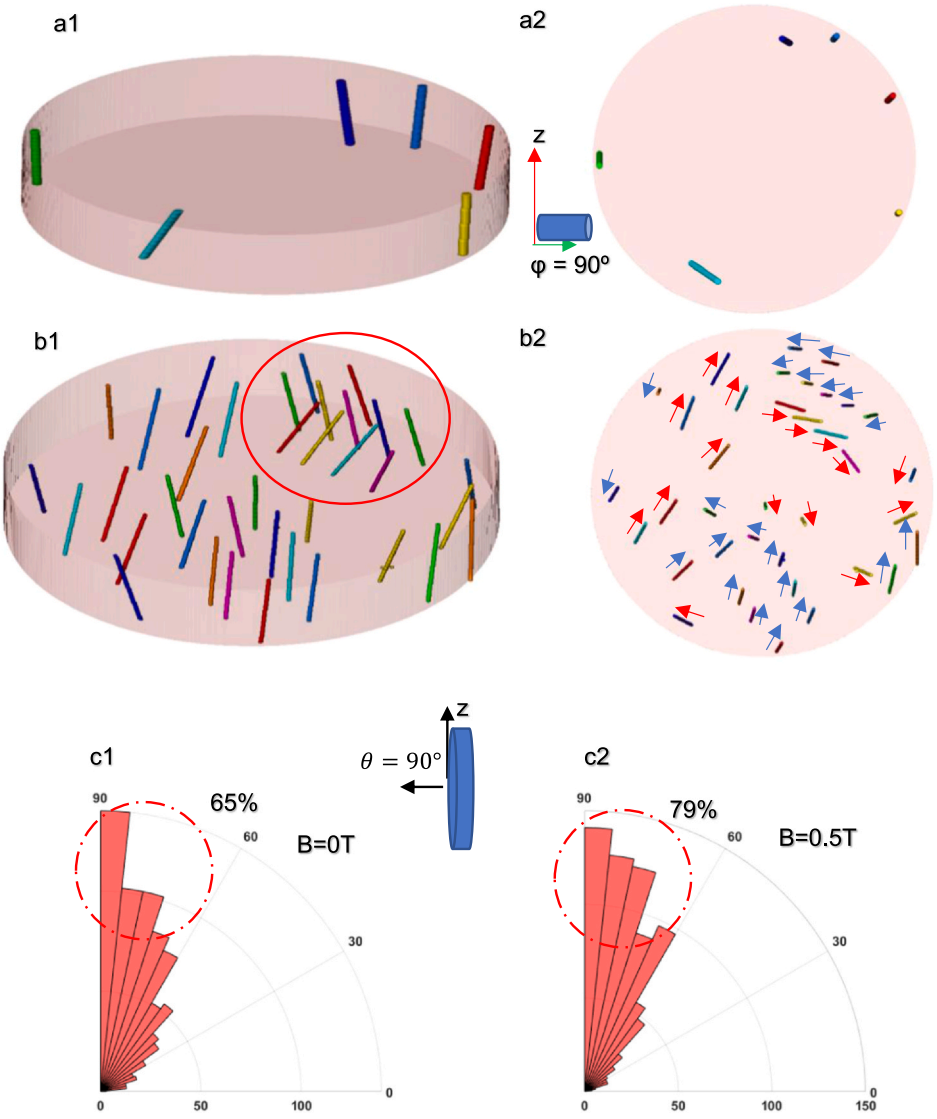


**Fig. 5.** (a) Growth orientations of α-phase (a) without magnetic field at ta0 + 64 s, side view (a1); top view (a2). (b) with magnetic field at ta0 + 64 s, side view (b1); top view (b2). (c) Growth orientations of β-phase (c1) without magnetic field at ta1 + 96 s; (c2) with magnetic field at tb1 + 96 s.

The horizontal cross-sections (Figs. 1-b5 and 2-b5) show a significant difference in dendrite sizes between the two different solidification conditions. Quantification of the primary dendritic arm spacing can be obtained by Eq. 1 [44]:

$$\lambda = c\sqrt{\frac{A}{n}} \tag{3}$$

Where $c$ is 0.5 for a random array of points, $A$ is the cross-section area, which is 4.54 mm$^2$ (Figs. 1-b5) and 4.72 mm$^2$ (Figs. 2-b5), respectively; $n$ is the number of dendrites, which are 6 (Figs. 1-b5) and 60 (Figs. 2-b5) for the two conditions, respectively. Therefore, the primary dendrite arm spacing solidified without and with a magnetic field is 435 µm and 140 µm, respectively.

### 3.2. *β-$Al_5FeSi$ intermetallic compounds (IMCs)*

Fig. 3-a shows the growth process of β-$Al_5FeSi$ IMCs at different timestamps under solidification condition I. $t_{a1}$ is the time when β-$Al_5FeSi$ IMCs first appeared in the FOV. The bright and thin-plate structure in Figs. 3-a2 is β-$Al_5FeSi$, which is the secondary phase after the primary α-Al phase formed in W319 alloys [20]. The light grey regions between the primary α-Al dendrites are liquid, whereas the dark grey is the α-Al phase. 3D volume rendering of IMCs after segmentation is shown in Fig. 3-b and video 3 at each corresponding time. The plate-shaped IMCs nucleated and grew first within the bottom of the FOV in Figs. 3-a1 and 3-b1. More IMCs nucleated at the top region (from Figs. 3-b2 to b4) at the later stage of solidification. A small volume (882× 882× 882 µm$^3$) was cropped out at the bottom of the FOV (red square in Figs. 3-a1) to provide better visualisation of IMCs, as presented in Figs. 3-c and 3d. The IMCs (in red) nucleated at the inter-dendritic space of primary α-Al phases (in green). β-$Al_5FeSi$ has very high lateral growth rates and low thickening rates, leading to impingement at the later stage of solidification. It also shows that the intermetallic compounds grew within the available spacing between the arms of the dendrites. Fig. 3-d presents the 3D volume of β-$Al_5FeSi$ while the primary α-Al phase is transparent. IMCs grew vertically towards the direction of the applied temperature gradient. Few IMCs grew horizontally.

Supplementary material related to this article can be found online at doi:10.1016/j.jallcom.2022.168691.

2D vertical slices and 3D rendered volumes of β-$Al_5FeSi$ at different timestamps under the magnetic field (solidification condition II) are shown in Fig. 4 and video-4. $t_{b1}$ is the time when β-$Al_5FeSi$ IMCs first appeared in the FOV. The growth behaviour of IMCs seems

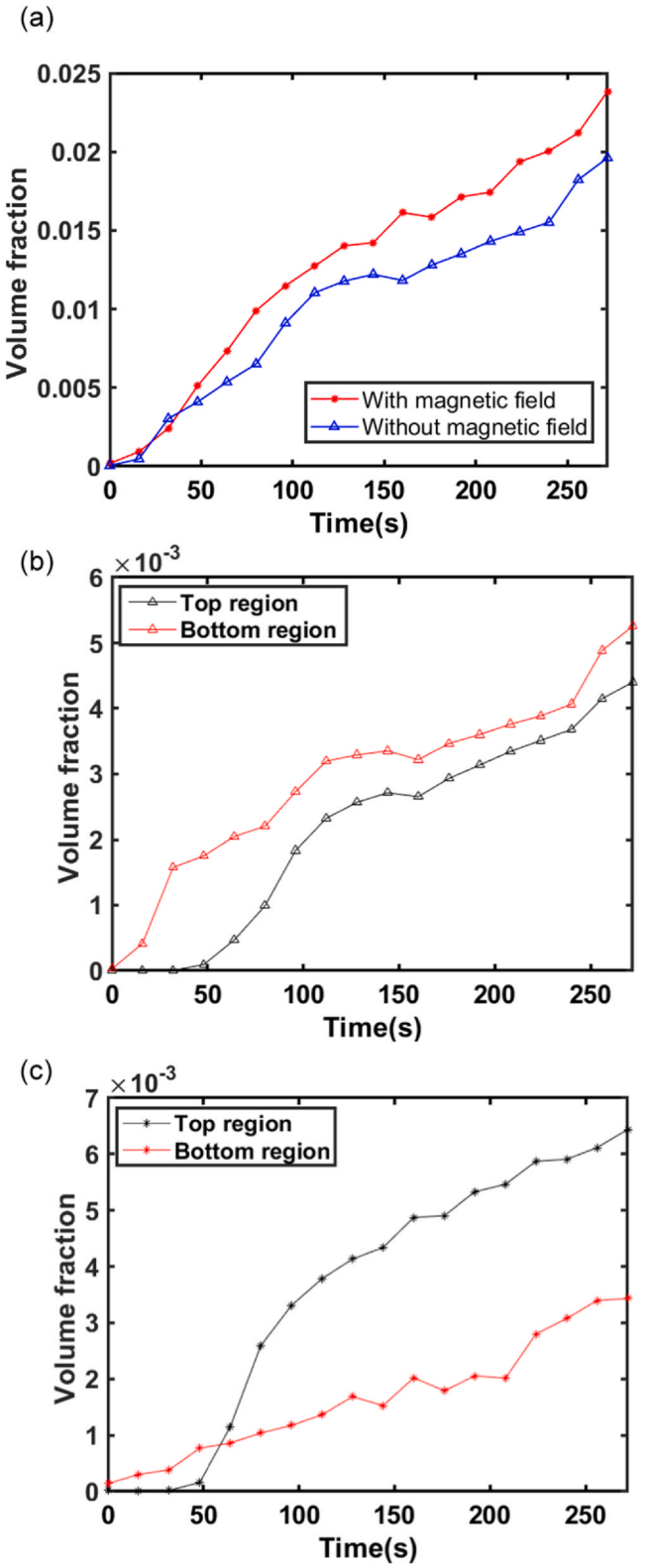


**Fig. 6.** (a) Overall volume fraction as a function of time; Volume fraction of β-phase at different height: (b) B= 0 T; (c) B= 0.5 T.

to be close to that of solidification condition I: (1) IMCs also nucleated at the bottom of the FOV and grew upwards (from Figs. 4-b1 to 4-b4), (II) Most of IMCs grew vertically.

Supplementary material related to this article can be found online at doi:10.1016/j.jallcom.2022.168691.

The growth orientation of IMCs was quantified based on the principal component analysis [20]. The angle $\theta$ was defined as the difference between the through-thickness direction of the plate-let intermetallics and the vertical direction of the sample (the schematic diagram is shown in the insert of Fig. 5-c, the z-axis is the vertical direction of the sample). Without the magnetic field, 65% of the IMCs grew between 60º and 90º in Fig. 5-a1, showing that the growth orientation of β-$Al_5FeSi$ preferably grew towards the vertical direction of the sample. The preferable growth direction towards the temperature gradient can be further influenced under a higher temperature gradient of 10℃/mm in ref [20]. When the magnetic field is on, a higher percentage of β-$Al_5FeSi$ IMCs (around 79%) grew between 60º to 90º in Fig. 5-a2. These indicate that the application of the magnetic field might affect the growth orientation of IMCs.

The volume fractions of β-phase versus time are plotted in Fig. 6-a. Without the magnetic field, the volume fraction of the β-phase gradually increased during solidification, with an average growth rate of about 0.7% per second. In 272 s, the volume fractions of β-phase achieved 1.9% which is consistent with a previous study [20]. The volume fraction of IMCs during solidification with the magnetic field grew at a rate of about 0.88% per second, slightly higher than the sample solidified without a magnetic field. The volume fraction increased to 2.4% in 272 s

Under the magnetic field, we noticed, in Figs. 4-b4, that the number of IMCs which grew at the bottom region of the FOV is lower than that at the top. We then quantified the volume fractions of the IMCs at the bottom (0–0.554 mm) and the top (1.662–2.216 mm) of the FOV as a function of time, as shown in Figs. 6-b and 6c. Fig. 6-b presents that the average growth rates (the tendency of the curves) of the IMCs of the bottom and top regions under solidification condition I are very close (about 0.0020% per second and 0.0018% per second, respectively). However, with the application of the magnetic field, the average growth rate of IMCs at the bottom region is 0.0013% per second, much slower than that at the top (0.0024% per second). The top region achieved a higher volume fraction (0.64%) than the bottom one (0.34%). The gradient volume distribution of the β-phase formed along the vertical direction of the FOV, suggesting the concentration of the Fe element might be higher at the top region than at the bottom. This behaviour is different from the sample solidified without the application of the magnetic field.

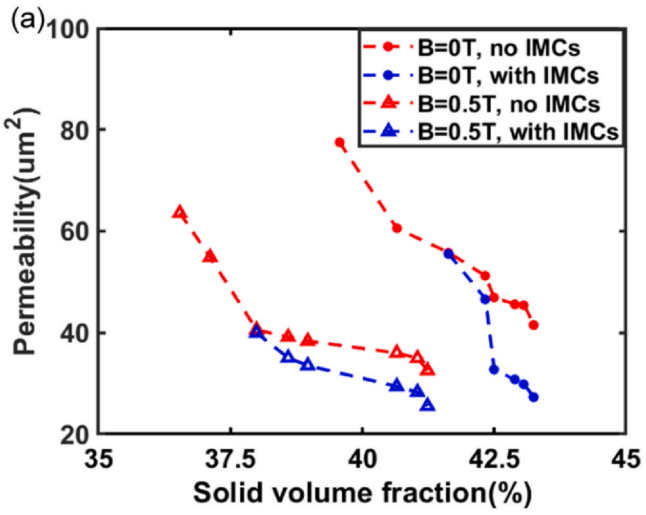


**Fig. 7.** (a) Simulated absolute permeability as a function of the solid volume fraction.

### 3.3. Permeability estimation

Fig. 7 presents the simulated absolute permeabilities of the semi-solid W319 alloys during solidification without and with the magnetic field, based on solving the Stokes equations. Without the magnetic field, the solid volume fraction of α-Al dendrites increased from 39.6% to 43.3% within the chosen 8 tomographic scans. The absolute permeabilities reduced from 77.6μm$^2$ to 41.6μm$^2$. The permeability decreased monotonically with the increase of solid volume fraction of α-Al dendrites as expected. The permeabilities are significantly lower in the presence of intermetallics, as was found by Puncreobutr et al., [21]. At a solid volume fraction of α-Al dendrites of 43.3%, the absolute permeability was 41.6 μm$^2$ without IMCs but reduced to 27.3μm$^2$ by the intermetallics. As the intermetallics nucleate and grow at the inter-dendritic spacing [19,20,45], they can block the liquid flow through the channels.

For solidification condition II, the permeability shows the same tendency. It decreased from 63.6μm$^2$ to 32.5μm$^2$ while the solid volume fraction increased from 36.5% to 41.2%. Permeability loss due to the presence of intermetallics also occurred. At a solid volume fraction of α-Al dendrites of 41.2%, the absolute permeability was 32.5 μm$^2$ without IMCs but was reduced to 25.6 μm$^2$ due to IMCs.

However, at the same solid volume fraction of α-Al phase of around 40.7%, the permeability is 60.5 μm$^2$ for the sample without the magnetic field applied, higher than the one with the magnetic field (36.0μm$^2$). The permeability is not only monotonically related to the volume fraction but can also be influenced by the inter-dendrite-arm spacing. Under the magnetic field, much finer dendrites were formed, resulting in narrower liquid channels. This can block melt to flow through the semi-solid structures, leading to lower absolute permeability. The reduction of primary dendrite arm spacing of the α-Al phase has a higher impact on the reduction of the absolute permeability than the blocking effect from the intermetallics.

### 3.4. Discussion

Fig. 8 shows the schematic diagram of the solidification process under both solidification conditions without and with the magnetic field. The presence of a magnetic field has changed the morphologies of the primary α-Al phase from coarse to fine dendritic structures. The distribution of the β-$Al_5FeSi$ IMCs was also altered.

Under solidification condition I without the magnetic field, initially, the primary α-Al was formed near the surface of the sample (Fig. 8-a1). Solute elements such as Cu, Fe and Si were ejected into the melt. Due to the gravity effect, heavy elements such as Cu and Fe settled down to the bottom of the FOV, forming a macro-segregation zone, which retards the upwards growth of the primary α-Al into this region. Therefore, a concavely curved solid/liquid interface was formed. As solidification progressed, the primary dendrite arms continued to grow upwards, while the secondary arms branched into

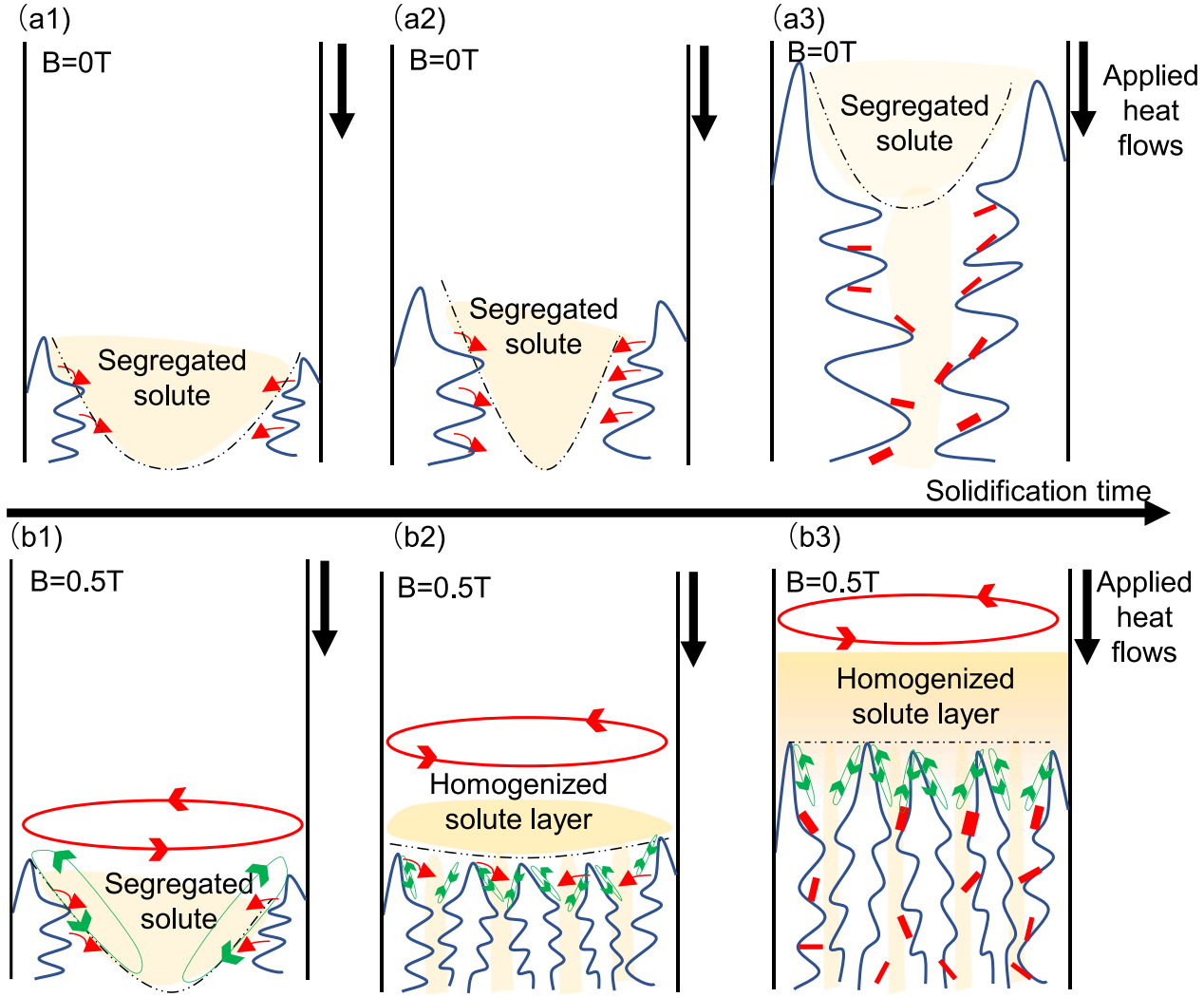


**Fig. 8.** Schematic diagram of the solidification process (a) without a transverse magnetic field; (b) under a transverse magnetic field while the sample was rotating.

the central region during cooling. The macro-segregation became more serious, which is because more Cu and Fe were ejected and accumulated into this region during solidification. The solid/liquid interface becomes more concave in Fig. 8-a2. The curved interface due to solute accumulation was observed previously in Al-Cu alloys [46] by examining the solidified sample, which for the first time demonstrated that fluid flow as a result of gravitational force can change the solid/liquid interface shape. In-situ X-ray radiography later was used by A. Bogno et al. [47] to reveal the initial transient of the solid/liquid interface due to solute segregation. As the solidification proceeded, the secondary β-IMCs started to nucleate and grew at the inter-dendritic spacing of the primary α-Al dendrites in Fig. 8-a3. The size of the secondary β-IMCs is constrained by the available spacing [20]. Its growth orientation is strongly controlled by the temperature gradient.

Under the magnetic field, initially, during solidification, the segregated heavy elements of Cu and Fe also accumulated at the centre region of the sample to form a curved solid/liquid interface in Figs. 2-a2 and schematically shown in Fig. 8-b1. A rotating magnetic field can induce a strong azimuthal flow that came from the convection damping effect [48,49]). Here, the sample was rotating under a transverse magnetic field. During solidification, the liquid flow was impeded due to the convection damping effect, while the solid α-Al dendrites were still rotating at angular velocity of π/s. Due to the speed difference between the liquid and solid part (α-Al dendrite), a rotational flow can be generated (in the red circle) in the mushy zone (Fig. 8-b1) in the direction of rotation.

Furthermore, due to the different electrical conductivities of the primary α-Al phase and the melt, current loops at the solid/liquid interface can be generated as shown in Fig. 8-b1 (in green), which is known as the Seebeck effect [22,33,50]. The interaction between the Seebeck current loops and the rotating magnetic field can induce Lorenz forces acting on both dendrites and the melt in the mushy zone. This can produce meridional flow ahead of the solid/liquid interface [51]. The changed interface from tilted to flat in Al-Cu alloys under a transverse magnetic field was observed by Wang et al. [52] by using in-situ radiography, and a corresponding 3D simulation was also performed to confirm that the changed interface was attributed to the induced thermoelectric magnetohydrodynamic flows (TEMHD) [53]. In their work, the sample was static, TEMHD alone was attributed to being the main mechanism for changing the solid/liquid interface. In our previous study, we observed the formation of a helical structure of the α-Al phase in Al-15 wt%Cu alloys, in which the screw structure was formed due to the formation of the helical channel enriched with Cu solute [26], suggesting that rotation inside a magnetic field can induce strong solute flow. In this experiment, the sample was also rotating inside a magnetic field. The combination of the two forces from the convection damping effect and TEMHD might homogenise the temperature distribution via mixing of the solute [26] and ease the macro-segregation, which allows more primary dendrites to grow into this region (Fig. 8-b2).

The solid/liquid interface transformed from a curved one to flat one during solidification. As a result of these combined magnetohydrodynamic effects, the number of dendrites was increased, and PDAS was reduced. Smaller PDAS led to narrower liquid channels, which can reduce the absolute permeability [21]. The refined primary dendrites led to the growth orientation of the IMCs towards the vertical direction of the sample. Finally, segregated solute was pushed above the solidified structures in Fig. 8-b3. This leads to a higher solute concentration at the top region of the sample, which promotes more β-$Al_5FeSi$ IMCs to form at the top region, resulting in a gradient volume distribution of IMCs [51]. This study demonstrates that applying a static magnetic field to a rotating sample can not only successfully reduce the PDAS but also alter the distribution of IMCs. It provides a cost-effective method for controlling the iron-rich intermetallic in recycled aluminium alloys and thus improving mechanical properties and corrosion resistance.

## 4. Conclusions

High-speed synchrotron X-ray tomography was used to reveal the growth dynamics of both the primary α-Al phase and secondary β-$Al_5FeSi$ IMCs in W319 alloys directionally solidified without and with a transversal magnetic field. This work reveals that the application of a transverse magnetic field during solidification processes can effectively change the morphology of the primary α-Al phase and subsequently alter the distribution of the secondary β-$Al_5FeSi$ IMCs. The following conclusions can be drawn from this study:

1. Without the magnetic field, a high concentration of heavy elements such as Cu and Fe at the periphery of the sample was revealed by mapping the solute distribution. Under a magnetic field, the peripheral macro-segregation was removed. A concave solid/liquid interface was observed at the initial stage of solidification under both conditions. However, the solid/liquid interface transformed from curved to flat when the magnetic field is applied.
2. Without the magnetic field, the primary α-Al phase has coarse and well-developed dendritic structures with large primary dendritic arm spacing of about 435 μm. Under the magnetic field, the primary α-Al phase becomes fine dendritic structures with smaller dendritic arm spacing of about 140 μm.
3. Absolute permeabilities were simulated using image-based simulation based on the tomographic data. The simulations show β-$Al_5FeSi$ IMCs can reduce the absolute permeability of the semi-solid structure by blocking flows in both solidification conditions. In addition, under an applied magnetic field, fine dendritic structures also reduce permeability due to the formation of narrower liquid channels.
4. Without a magnetic field, the volume fraction and growth rate of β-$Al_5FeSi$ IMCs have almost the same values at different regions of the sample. However, under the magnetic field, at the top region of the sample, the β-$Al_5FeSi$ IMCs have higher growth rates and volume fractions than the bottom.

## CRediT authorship contribution statement

**Zihan Song**: Writing – original draft, Methodology, Formal analysis, Validation, Investigation. **Elodie Boller**: Validation, Investigation. **Alexander Rack**: Validation, Investigation, Writing – review & editing. **Peter D. Lee**: Investigation, Validation, Writing – review & editing. **Biao Cai**: Writing – review & editing, Validation, Investigation, Conceptualization, Supervision, Funding acquisition.

## Data availability

Data will be made available on request.

## Declaration of Competing Interest

The authors declare that they have no known competing financial interests or personal relationships that could have appeared to influence the work reported in this paper.

## Acknowledgement

Z.S. thanks the UK-EPSRC CDT Grant (No: EP/L016206/1) in Innovative Metal Processing for financial support. B.C. acknowledges the UKRI Future Leaders Fellowship (MR/W007967/1) for support. P.D.L. acknowledges a Royal Academy of Engineering Chair in

Emerging Technology (CiET1819/10). The authors gratefully acknowledge the European Synchrotron Radiation Facility for Beamtime MA2989 and the ID19 team and collaborators who helped with the experiments.

## Appendix A. Supporting information

Supplementary data associated with this article can be found in the online version at doi:10.1016/j.jallcom.2022.168691.

## References


[1] S.K. Das, W. Yin, The worldwide aluminum economy: the current state of the industry, Jom 59 (2007) 57–63, https://doi.org/10.1007/s11837-007-0142-0

[2] D. Wang, X. Zhang, H. Nagaumi, X. Li, H. Zhang, 3D morphology and growth mechanism of cubic a -Al ( FeMnCr) Si intermetallic in an Al-Si cast alloy, Mater. Lett. 277 (2020) 128384, https://doi.org/10.1016/j.matlet.2020.128384

[3] J.A. Taylor, Iron-containing intermetallic phases in Al-Si based casting alloys, Procedia Mater. Sci. 1 (2012) 19–33, https://doi.org/10.1016/j.mspro.2012.06.004

[4] S. Feng, Y. Cui, E. Liotti, A. Lui, C.M. Gourlay, P.S. Grant, In-situ X-ray radiography of twinned crystal growth of primary Al13Fe4, Scr. Mater. 184 (2020) 57–62, https://doi.org/10.1016/j.scriptamat.2020.04.010

[5] Y. Zhao, W. Zhang, D. Song, B. Lin, F. Shen, D. Zheng, C.X. Xie, Z. Sun, Y. Fu, R. Li, Nucleation and growth of Fe-rich phases in Al-5Ti-1B modified Al-Fe alloys investigated using synchrotron X-ray imaging and electron microscopy, J. Mater. Sci. Technol. 80 (2021) 84–99, https://doi.org/10.1016/j.jmst.2020.12.011

[6] L. Zhang, W. Jing, Y. Yang, H. Yang, Y. Guo, H. Sun, J. Zhao, J. Yao, The investigation of permeability calculation using digital core simulation technology, Energies 12 (2019) 1–9, https://doi.org/10.3390/en12173273

[7] E. Taghaddos, M.M. Hejazi, R. Taghiabadi, S.G. Shabestari, Effect of iron-intermetallics on the fluidity of 413 aluminum alloy, J. Alloy. Compd. 468 (2009) 539–545, https://doi.org/10.1016/j.jallcom.2008.01.079

[8] S. Ji, W. Yang, F. Gao, D. Watson, Z. Fan, Effect of iron on the microstructure and mechanical property of Al-Mg-Si-Mn and Al-Mg-Si diecast alloys, Mater. Sci. Eng. A 564 (2013) 130–139, https://doi.org/10.1016/j.msea.2012.11.095

[9] Z. Ma, A.M. Samuel, F.H. Samuel, H.W. Doty, S. Valtierra, A study of tensile properties in Al-Si-Cu and Al-Si-Mg alloys: effect of β-iron intermetallics and porosity, Mater. Sci. Eng. A 490 (2008) 36–51, https://doi.org/10.1016/j.msea.2008.01.028

[10] D.G. Eskin, J. Mi, Solidication Processing of Metallic Alloys Under External fields, Springer, Cham, Switzerland, 2018, https://doi.org/10.1007/978-3-319-94842-3

[11] F. Wang, D. Eskin, J. Mi, C. Wang, B. Koe, A. King, C. Reinhard, T. Connolley, A synchrotron X-radiography study of the fragmentation and refinement of primary intermetallic particles in an Al-35 Cu alloy induced by ultrasonic melt processing, Acta Mater. 141 (2017) 142–153, https://doi.org/10.1016/j.actamat.2017.09.010

[12] T. Manuwong, W. Zhang, P.L. Kazinczi, A.J. Bodey, C. Rau, J. Mi, Solidification of Al alloys under electromagnetic pulses and characterization of the 3D microstructures using synchrotron X-ray tomography, Metall. Mater. Trans. A Phys. Metall. Mater. Sci. 46 (2015) 2908–2915, https://doi.org/10.1007/s11661-015-2874-8

[13] Z. Zhang, C. Wang, B. Koe, C.M. Schlepütz, S. Irvine, J. Mi, Synchrotron X-ray imaging and ultrafast tomography in situ study of the fragmentation and growth dynamics of dendritic microstructures in solidification under ultrasound, Acta Mater. (2021) 116796, https://doi.org/10.1016/j.actamat.2021.116796

[14] Z. Song, O.V. Magdysyuk, T. Sparks, Y. Chiu, B. Cai, Revealing growth mechanisms of faceted Al2Cu intermetallic compounds via high-speed Synchrotron X-ray tomography, Acta Mater. (2022) 117903, https://doi.org/10.1016/j.actamat.2022.117903

[15] A. Bjurenstedt, D. Casari, S. Seifeddine, R.H. Mathiesen, A.K. Dahle, In-situ study of morphology and growth of primary α-Al(FeMnCr)Si intermetallics in an Al-Si alloy, Acta Mater. 130 (2017) 1–9, https://doi.org/10.1016/j.actamat.2017.03.026

[16] S. Feng, E. Liotti, A. Lui, M.D. Wilson, T. Connolley, R.H. Mathiesen, P.S. Grant, In-situ X-ray radiography of primary Fe-rich intermetallic compound formation, Acta Mater. 196 (2020) 759–769, https://doi.org/10.1016/j.actamat.2020.06.045

[17] B. Cai, J. Wang, A. Kao, K. Pericleous, A.B. Phillion, R.C. Atwood, P.D. Lee, 4D synchrotron X-ray tomographic quantification of the transition from cellular to dendrite growth during directional solidification, Acta Mater. 117 (2016) 160–169, https://doi.org/10.1016/j.actamat.2016.07.002

[18] Z. Song, O. Magdysyuk, L. Tang, T. Sparks, B. Cai, Growth dynamics of faceted Al13Fe4 intermetallic revealed by high-speed synchrotron X-ray quantification, J. Alloy. Compd. 861 (2021) 1–15, https://doi.org/10.1016/j.jallcom.2021.158604

[19] S. Terzi, J.A. Taylor, Y.H. Cho, L. Salvo, M. Suéry, E. Boller, A.K. Dahle, In situ study of nucleation and growth of the irregular α-Al/β-Al5FeSi eutectic by 3-D synchrotron X-ray microtomography, Acta Mater. 58 (2010) 5370–5380, https://doi.org/10.1016/j.actamat.2010.06.012

[20] B. Cai, A. Kao, P.D. Lee, E. Boller, H. Basevi, A.B. Phillion, A. Leonardis, K. Pericieous, Growth of β intermetallic in an Al-Cu-Si alloy during directional solidification via machine learned 4D quantification, Scr. Mater. 165 (2019) 29–33, https://doi.org/10.1016/j.scriptamat.2019.02.007

[21] C. Puncreobutr, A.B. Phillion, J.L. Fife, P.D. Lee, Coupling in situ synchrotron X-ray tomographic microscopy and numerical simulation to quantify the influence of intermetallic formation on permeability in aluminium–silicon–copper alloys, Acta Mater. 64 (2014) 316–325, https://doi.org/10.1016/j.actamat.2013.10.044

[22] J. Cao, S. Shuai, C. Huang, T. Hu, C. Chen, J. Wang, Z. Ren, 4D synchrotron X-ray tomographic study of the influence of transverse magnetic field on iron intermetallic compounds precipitation behavior during solidification of Al–Si–Fe alloy, Intermetallics 143 (2022) 107471, https://doi.org/10.1016/j.intermet.2022.107471

[23] X. Li, Y. Fautrelle, Z. Ren, R. Moreau, Formation mechanism of axial macrosegregation of primary phases induced by a static magnetic field during directional solidification, Sci. Rep. 7 (2017) 1–13, https://doi.org/10.1038/srep45834

[24] S. Hu, L. Hou, K. Wang, Z. Liao, Y. Fautrelle, W. Li, X. Li, Formation mechanism of gradient structure of aluminum matrix composite under static magnetic field during directional solidification, J. Mater. Res. Technol. 9 (2020) 4459–4468, https://doi.org/10.1016/j.jmrt.2020.02.072

[25] S. Shuai, X. Lin, Y. Dong, L. Hou, H. Liao, J. Wang, Z. Ren, Three dimensional dendritic morphology and orientation transition induced by high static magnetic field in directionally solidified Al-10 wt%Zn alloy, J. Mater. Sci. Technol. 35 (2019) 1587–1592, https://doi.org/10.1016/j.jmst.2019.03.029

[26] B. Cai, A. Kao, E. Boller, O.V. Magdysyuk, R.C. Atwood, N.T. Vo, K. Pericleous, P.D. Lee, Revealing the mechanisms by which magneto-hydrodynamics disrupts solidification microstructures, Acta Mater. 196 (2020) 200–209, https://doi.org/10.1016/j.actamat.2020.06.041

[27] N. Shevchenko, O. Roshchupkina, O. Sokolova, S. Eckert, The effect of natural and forced melt convection on dendritic solidification in Ga-In alloys, J. Cryst. Growth 417 (2015) 1–8, https://doi.org/10.1016/j.jcrysgro.2014.11.043

[28] F. Cao, F. Yang, H. Kang, C. Zou, T. Xiao, W. Huang, T. Wang, Effect of traveling magnetic field on solute distribution and dendritic growth in unidirectionally solidifying Sn–50 wt%Pb alloy: an in situ observation, J. Cryst. Growth 450 (2016) 91–95, https://doi.org/10.1016/j.jcrysgro.2016.06.034

[29] W. Ren, Z. Ren, K. Deng, Y. Zhong, Z. Lei, X. Li, Progress in research on solidification in a strong static magnetic field, Steel Res. Int. 78 (2007) 373–378, https://doi.org/10.1002/srin.200705906

[30] W.L. Ren, Y.F. Fan, J.W. Feng, Y.B. Zhong, J.B. Yu, Z.M. Ren, P.K. Liaw, Non-monotonic changes in critical solidification rates for stability of liquid-solid interfaces with static magnetic fields, Sci. Rep. 6 (2016) 2–11, https://doi.org/10.1038/srep20598

[31] S. Agrawal, A.K. Ghose, I. Chakrabarty, Effect of rotary electromagnetic stirring during solidification of In-situ Al-TiB2 composites, Mater. Des. 113 (2017) 195–206, https://doi.org/10.1016/j.matdes.2016.10.007

[32] S. Nafisi, D. Emadi, M.T. Shehata, R. Ghomashchi, Effects of electromagnetic stirring and superheat on the microstructural characteristics of Al-Si-Fe alloy, Mater. Sci. Eng. A 432 (2006) 71–83, https://doi.org/10.1016/j.msea.2006.05.076

[33] J.A. Shercliff, Thermoelectric magnetohydrodynamics, Phys. Fluids 22 (1979) 635–640, https://doi.org/10.1063/1.862646

[34] X. Li, Y. Fautrelle, Z. Ren, Influence of thermoelectric effects on the solid–liquid interface shape and cellular morphology in the mushy zone during the directional solidification of Al–Cu alloys under a magnetic field, Acta Mater. 55 (2007) 3803–3813, https://doi.org/10.1016/j.actamat.2007.02.031

[35] G. Zimmermann, V.T. Vitusevych, L. Sturz, Microstructure formation in AlSi6Cu4 alloy with forced melt flow induced by a rotating magnetic field, Mater. Sci. Forum 649 (2010) 249–254, https://doi.org/10.4028/www.scientific.net/MSF.649.249

[36] M. Javidani, D. Larouche, Application of cast Al-Si alloys in internal combustion engine components, Int. Mater. Rev. 59 (2014) 132–158, https://doi.org/10.1179/1743280413Y.0000000027

[37] T. Nelson, B. Cai, N. Warnken, P.D. Lee, E. Boller, O.V. Magdysyuk, N.R. Green, Gravity effect on thermal-solutal convection during solidification revealed by four-dimensional synchrotron imaging with compositional mapping, Scr. Mater. 180 (2020) 29–33, https://doi.org/10.1016/j.scriptamat.2019.12.026

[38] M. Drakopoulos, T. Connolley, C. Reinhard, R. Atwood, O. Magdysyuk, N. Vo, M. Hart, L. Connor, B. Humphreys, G. Howell, S. Davies, T. Hill, G. Wilkin, U. Pedersen, A. Foster, N. De Maio, M. Basham, F. Yuan, K. Wanelik, J. Synchrotron Radiat. 22 (2015) 828–838, https://doi.org/10.1107/S1600577515003513

[39] C. Puncreobutr, A.B. Phillion, J.L. Fife, P. Rockett, A.P. Horsfield, P.D. Lee, In situ quantification of the nucleation and growth of Fe-rich intermetallics during Al alloy solidification, Acta Mater. 79 (2014) 292–303, https://doi.org/10.1016/j.actamat.2014.07.018

[40] B. Cai, P.D. Lee, S. Karagadde, T.J. Marrow, T. Connolley, Time-resolved synchrotron tomographic quantification of deformation during indentation of an equiaxed semi-solid granular alloy, Acta Mater. 105 (2016) 338–346, https://doi.org/10.1016/j.actamat.2015.11.028

[41] E. Guo, A.B. Phillion, B. Cai, S. Shuai, D. Kazantsev, T. Jing, P.D. Lee, Dendritic evolution during coarsening of Mg-Zn alloys via 4D synchrotron tomography, Acta Mater. 123 (2017) 373–382, https://doi.org/10.1016/j.actamat.2016.10.022

[42] A. Nobuyuki Otsu, Threshold selection method from Gray-Level Histograms, IEEE Trans. Syst. Man Cybern. 9 (1979) 62–66.

[43] R. March, XXIX. An experimental investigation of the circumstances which determine whether the motion of water shall be direct or sinuous, and of the law of resistance in parallel channels, Philos. Trans. R. Soc. Lond. 174 (1883) 935–982, https://doi.org/10.1098/rstl.1883.0029

[44] M.A. Tschopp, J.D. Miller, A.L. Oppedal, K.N. Solanki, Characterizing the local primary dendrite arm spacing in directionally solidified dendritic microstructures, Metall. Mater. Trans. A Phys. Metall. Mater. Sci. 45 (2014) 426–437, https://doi.org/10.1007/s11661-013-1985-3

[45] J.S. Wang, P.D. Lee, In-situ observation and mathematical modelling of the nucleation and growth of intermetallics and micropores during the solidification of aluminium alloys, Dep. Mater. PhD (2009).
[46] M.H. Burden, D.J. Hebditch, J.D. Hunt, Macroscopic stability of a planar, cellular or dendritic interface during directional freezing, J. Cryst. Growth 20 (1973) 121–124, https://doi.org/10.1016/0022-0248(73)90125-5
[47] A. Bogno, H. Nguyen-Thi, A. Buffet, G. Reinhart, B. Billia, N. Mangelinck-Noël, N. Bergeon, J. Baruchel, T. Schenk, Analysis by synchrotron X-ray radiography of convection effects on the dynamic evolution of the solid-liquid interface and on solute distribution during the initial transient of solidification, Acta Mater. 59 (2011) 4356–4365, https://doi.org/10.1016/j.actamat.2011.03.059
[48] P. Mikolajczak, L. Ratke, Effect of stirring induced by rotating magnetic field on β-Al5FeSi intermetallic phases during directional solidification in AlSi alloys, Int. J. Cast. Met. Res. 26 (2013) 339–353, https://doi.org/10.1179/1743133613Y.0000000069
[49] H. Zhang, M. Wu, Z. Zhang, A. Ludwig, A. Kharicha, A. Rónaföldi, A. Roósz, Z. Veres, M. Svéda, Experimental evaluation of MHD modeling of EMS during continuous casting, Metall. Mater. Trans. B (2022), https://doi.org/10.1007/s11663-022-02516-3
[50] A. Kao, B. Cai, P.D. Lee, K. Pericleous, The effects of Thermoelectric Magnetohydrodynamics in directional solidification under a transverse magnetic field, J. Cryst. Growth 457 (2017) 270–274, https://doi.org/10.1016/j.jcrysgro.2016.07.003
[51] H. Zhang, M. Wu, C.M.G. Rodrigues, A. Ludwig, A. Kharicha, Directional solidification of AlSi7Fe1 alloy under forced flow conditions: effect of intermetallic phase precipitation and dendrite coarsening, Metall. Mater. Trans. A Phys. Metall. Mater. Sci. 52 (2021) 3007–3022, https://doi.org/10.1007/s11661-021-06295-5
[52] J. Wang, Y. Fautrelle, Z.M. Ren, H. Nguyen-Thi, G. Salloum Abou Jaoude, G. Reinhart, N. Mangelinck-Noël, X. Li, I. Kaldre, Thermoelectric magnetic flows in melt during directional solidification, Appl. Phys. Lett. 104 (2014), https://doi.org/10.1063/1.4870099
[53] J. Wang, Y. Fautrelle, H. Nguyen-Thi, G. Reinhart, H. Liao, X. Li, Y. Zhong, Z. Ren, Thermoelectric magnetohydrodynamic flows and their induced change of solid–liquid interface shape in static magnetic field-assisted directional solidification, Metall. Mater. Trans. A Phys. Metall. Mater. Sci. 47 (2016) 1169–1179, https://doi.org/10.1007/s11661-015-3277-6